

# External and internal controls on decadal precipitation variability over North America

Xiaolu Fan<sup>1</sup> · Jianping Huang<sup>2</sup> · Yongkun Xie<sup>2</sup> · Wenmin Wei<sup>1</sup> · Yu Ren<sup>1</sup> · Yihui Xu<sup>1</sup> · Ming Peng<sup>1</sup> · Li Fu<sup>1</sup>

Received: 21 March 2025 / Accepted: 17 October 2025 © The Author(s), under exclusive licence to Springer-Verlag GmbH Germany, part of Springer Nature 2025

#### **Abstract**

The profound impacts of North American (NA) precipitation variability on drought, agriculture, and society make understanding its external and internal drivers critically important. However, most studies have focused on either external forcing or internal variability in specific NA regions, neglecting their combined effects across the entire continent. Here, we combine long-term observational data and CMIP6 simulations to find the distinct roles of anthropogenic forcing and low-frequency internal variability. Results reveal a long-term wetting trend primarily driven by greenhouse gas forcing, though systematically underestimated by models. Decadal precipitation oscillations are modulated by internal variability, especially the Interdecadal Pacific Oscillation (IPO), whose sea surface temperature anomalies trigger Rossby waves that alter moisture transport and establish a tripolar precipitation pattern. This pattern dominates NA precipitation variability at decadal scales, surpassing anthropogenic influences. From 2021 to 2050, the tripolar pattern is projected to persist, contingent on IPO phase. By 2100, constrained projections under the SSP2-4.5 and SSP5-8.5 scenarios suggest a further intensification of precipitation increases. This study shows how NA rainfall responds differently to human influence and natural oscillations over decades, with implications for improving our ability to predict and attribute regional climate changes.

Keywords Decadal precipitation variability · North America · External forcing · Internal variability

# 1 Introduction

Precipitation variability across North America (NA) substantially impacts regional water resource security, agricultural productivity, ecosystem stability, and the frequency of extreme climatic events (Grigg 2014; Littell et al. 2016; Chikamoto et al. 2017; Sugg et al. 2020). The variation in annual precipitation plays a critical role in drought events and the expansion of drylands (Feng and Fu 2013; Seager and Hoerling 2014; Seager and Ting 2017). Previous studies have documented that both anthropogenic forcing and internal variability have been identified as factors influencing NA precipitation changes (Ault and George 2010; Hu and Feng 2012; Zhang et al. 2024). However, the interplay

between the two factors is complex. Huang et al. (2016) indicate a persistent tripolar precipitation pattern over NA during 1948–2005, which resulted in drying tendencies across most Canadian regions (excluding the northeast), while contributing to the widespread wetting trends over the United States. The relative contributions of external forcing and internal variability to the driving mechanisms of this spatial pattern over NA remain unclear. Therefore, distinguishing the impacts of external forcing and internal variability is crucial for understanding past precipitation changes over NA and improving future projections for the region.

Increased greenhouse gas concentrations can raise temperatures, enhancing the moisture-holding capacity of the near-surface atmosphere according to the Clausius-Clapeyron relation (Easterling et al. 2017; Prein et al. 2017). Precipitation has already exhibited a positive response to greenhouse gas emissions (Held and Soden 2006; Stephens and Ellis 2008; Pendergrass and Hartmann 2014). The influence of external forcing on regional precipitation variability has been extensively studied (Liu et al. 2023; Huang et al. 2023; Jiang et al. 2023). Regarding the NA region, external

Published online: 03 November 2025



<sup>☑</sup> Jianping Huang hjp@lzu.edu.cn

College of Atmospheric Sciences, Lanzhou University, Lanzhou 730000, China

Collaborative Innovation Center for Western Ecological Safety, Lanzhou University, Lanzhou 730000, China

forcing has contributed to both extreme precipitation intensification and the observed century-scale wetting trend across the northeastern United States (Kunkel et al. 2013; Agel and Barlow 2020). The mid-Atlantic region of the United States exhibits increased wetness during both summer and winter seasons, driven predominantly by external forcing factors (Dong and Leung 2022). Studies have demonstrated that in the west coastal regions of NA, the intensification of precipitation becomes more pronounced with increasing warming (Ma et al. 2020). Despite these insights, studies remain focused on specific regions, and a comprehensive understanding of externally forced precipitation changes across all of NA over the past century is still lacking.

In addition to external forcing, internal variability through various large-scale teleconnection patterns plays a critical role in modulating precipitation changes over NA, particularly on interannual to decadal scales. The Rossby waves triggered by El Niño and Southern Oscillation (ENSO) propagate along the great circle, moving poleward and eastward, and generate quasi-stationary circulation anomalies resembling the Pacific-North American (PNA) pattern, which alters the Pacific storm track and facilitates moisture transport toward NA (Wallace and Gutzler 1981; Leathers et al. 1991; Seager et al. 2005; Chen et al. 2018). On decadal time scales, low-frequency variability in the tropical Pacific, such as the Interdecadal Pacific Oscillation (IPO), significantly influences precipitation patterns over NA (McCabe et al. 2004; Hayhoe et al. 2007; Dai 2013; Xu and Hu 2018; Dong et al. 2021). The Atlantic Multidecadal Oscillation (AMO) also influences NA precipitation on decadal time scales (Enfeld et al. 2001; Kushnir et al. 2010; Ruprich-Robert et al. 2018; Johnson et al. 2020; Huang et al. 2021). Yet, most studies cover only one or two full cycles of the AMO/IPO, limiting robust assessment of their decadal-scale influence on NA climate variability.

Although significant progress has been made in understanding the precipitation changes over NA, the comprehensive attribution of annual precipitation changes to external forcing and internal variability remains poorly understood. At regional scales, if the observational record is insufficiently long, the climate system's internal variability may mask anthropogenic signals (Huang et al. 2020; Wu et al. 2021; Zhang et al. 2024). Therefore, this study utilizes longterm precipitation data from CMIP6 models and observations, applying optimal fingerprint detection techniques to analyze the climatic impacts of anthropogenic forcing and internal variability, and compare their respective roles. Furthermore, this study provides projections of decadal variability and long-term trends in future precipitation over NA. The remainder of this paper is arranged into five parts. Section 2 provides a detailed description of the datasets and methods used in this paper. Section 3 investigates the leading modes of precipitation and quantifies the contributions of external forcing. Section 4 elucidates the influence mechanisms of oceanic variability on precipitation. Section 5 presents projections of future changes in precipitation over NA. Discussion and conclusion are offered in Sect. 6.

### 2 Data sets and methods

#### 2.1 Data

We used two precipitation datasets to confirm the robustness of decadal and long-term precipitation changes over NA. Both datasets have sufficiently long time scales: (1) a monthly precipitation dataset from the Climatic Research Unit (CRU) v4.05 with a 0.5° horizontal resolution covering the period from 1901 to 2020 provided by the University of East Anglia (Harris et al. 2014). (2) a monthly precipitation dataset provided by the Global Precipitation Climatology Centre (GPCC) (Schneider et al. 2014) with a 0.5° horizontal resolution from 1891 to 2020. The Extended Reconstructed Sea Surface Temperature (ERSST) dataset provided by National Oceanic and Atmospheric Administration (NOAA) Extended Reconstruction SST Version 5 (ERSSTv5), begins in January 1854 continuing to the present, in grids of 2°horizontal resolution. The reanalysis dataset used in this study is derived from Twentieth Century Reanalysis version V3 (20CRV3) (Slivinski et al. 2021). The horizontal resolution of 20CRV3 reanalysis data is 1°. The 20CRV3 data was only updated to 2015. The data was extended to 2020 using NCEP-DOE Reanalysis 2 (Kanamitsu et al. 2002). The atmospheric datasets employed in this study include geopotential height (z), specific humidity (q), vertical velocity (omega) and horizontal winds (u, v) at pressure levels.

#### 2.2 Methods

# 2.2.1 Oceanic variability

The IPO index is defined as the detrended SST averaged over the tropical central-eastern Pacific (10° S–10° N, 170°–90° W) minus the detrended SST averaged over the northern Pacific (25°–45° N, 150° E–150° W), similar to a previous study (Cai et al. 2024). The AMO index (Trenberth and Shea 2006) is a detrended time series, defined as regionally weighted mean values of SST in the North Atlantic from (0°–70° N, 80° W–0°). The empirical orthogonal function (EOF) method was used to extract the IPO and AMO spatial patterns (Extended Data Fig. 2a, c).



#### 2.2.2 Leading modes of NA precipitation

The two leading modes of annual precipitation over NA are obtained through EOF analysis in the 11°-70°N, 170°-53°W region. We use normalized annual precipitation anomalies to conduct the EOF analysis, and then the original precipitation amount is regressed onto the corresponding time series to obtain the spatial pattern. The results of EOF analysis are well separated from other modes according to North test (North et al. 1982).

# 2.2.3 Model simulations

To investigate the role of external forcing in precipitation variability over NA, this study utilizes multimodel simulations from the Detection and Attribution Model Intercomparison Project (DAMIP) under the Coupled Model Intercomparison Project Phase 6 (CMIP6). Combined and individual forcing are considered, including all external forcing (ALL, including both anthropogenic and natural forcing), with all external forcing simulations covering a period from 1850 to 2014 and are extended to 2020 using the Shared Socioeconomic Pathway 2-Representative Concentration Pathway 4.5 (SSP2-4.5) emission scenario, natural forcing alone (NAT), greenhouse gas forcing alone (GHG), anthropogenic aerosol-only forcing (AA), and anthropogenic forcing alone (ANT, ALL-NAT) covering a period from 1850 to 2020. A total of 10 CMIP6 models are used because they can capture the rainfall characteristics of NA in the climatological mean (Extended Data Fig. 9). For each model, all realizations are included, resulting in 125 realizations for ALL forcing, 100 for NAT forcing, 93 for GHG forcing, and 125 for ANT forcing. To evaluate future precipitation changes, projections under both the SSP2-4.5 and SSP5-8.5 scenarios are also incorporated, covering the period from 2015 to 2100 (Extended Data Table 1). The ACCESS-ESM1-5 and MIROC6 models provide a sufficient number of realizations (>40) for both historical simulations and future projections under the SSP2-4.5 and SSP5-8.5 scenarios. Additionally, MIROC6 offers single-forcing projections under the SSP2-4.5 scenario (see Extended Data Table 1). For the analysis of spatial patterns and optimal fingerprint detection, all simulations are regridded to a common 1° horizontal resolution.

#### 2.2.4 Optimal fingerprint detection and attribution

We employed an optimal fingerprinting method to attribute the influence of external forcing (Allen and Stott 2003; Ribes et al. 2017), which is based on a generalized multivariate linear regression model (Zhang et al. 2007, 2019). It is expressed as  $y=\beta(X-\mu)+\epsilon$ . Observed changes (y) are represented as a sum of various external (X) ("fingerprints")

drivers, plus the noise that cannot be explained by the external forcing (ε). Because of finite-ensemble simulations, the sampling noise  $(\mu)$  arises in the estimation of (X). The ordinary least squares (OLS) regression was used here (Allen and Tett 1999; Douville et al. 2013; Wang et al. 2020; Sun et al. 2022). The scaling factor (β) plays a key role in determining the magnitude of the response to a specific external forcing in climate modeling. It adjusts the modeled response to best match the observed data, ensuring that the effects of the external forcing are accurately represented. A scaling factor (B) significantly larger than zero, with its 90% confidence interval excluding zero, indicates that the influence of a particular forcing can be detected in the observed changes. Additionally, when the scaling factor  $(\beta)$  exceeds 1, it suggests that the ensemble simulations are underrepresenting the observed response, while the opposite is true when the scaling factor is less than 1. In this study, the regularized optimal fingerprinting method is applied (Allen and Tett 1999; Sun et al. 2022; Wang et al. 2020; Jiang et al. 2023), which operates without depending on EOF decomposition.

In this research, the optimal fingerprinting method is applied to the area-averaged precipitation over NA from 1901 to 2020. Both the simulated and observed data are regridded to a 1° horizontal resolution prior to the regression analysis. To enhance the signal-to-noise ratio, the time series is processed using a non-overlapping 5-year moving average, resulting in 24 data points that filter out interannual variability.

Two separate sources are used to estimate internal variability (noise) in order to expand the sample size: preindustrial control simulations and intra-ensemble spread from single-forcing runs. The internal variability is derived from these two datasets, which collectively enhance the reliability of the estimation. In the single-forcing analysis, we performed a regression of the observed vector onto the simulated vector for each individual external forcing (e.g.,  $y = \beta_{GHG}(X_{GHG} - \mu_{GHG}) + \epsilon$ ).

# 2.2.5 Observationally constrained projections

Following the methodology of Zhang et al. (2007), the warming trends attributed to external forcing are estimated by multiplying the corresponding scaling factors. To address potential underestimation of the model's response to external forcing, we used the scaling factor derived from the one-signal analysis as constraints for future projections of precipitation, following the approach outlined in previous studies (Sun et al. 2014).



429 Page 4 of 15 X. Fan et al.

## 2.2.6 Dynamic mechanism diagnostic methods

The eddy stream function and Plumb wave activity flux were used to examine the stationary Rossby wave trains. The eddy stream function indicates that the zonal mean of the stream function was removed. The Plumb wave activity flux was calculated based on the formula (7.1) in Plumb (1985).

To understand the dynamic and thermodynamic mechanisms responsible for the GHG forcing, we conducted a moisture budget diagnostic analysis using the atmospheric water budget equation (Seager and Vecchi 2010; Chou and Lan 2012; Ren et al. 2024), as outlined below:

$$P - E = -\langle V_h \cdot \nabla_h q \rangle - \langle \omega \partial_p q \rangle + res \tag{1}$$

Climatologically, precipitation (P) is balanced by evaporation (E), vertical moisture advection  $(-<\omega\partial_pq>)$  and horizontal moisture advection  $(-< V_h \cdot \nabla_h q>)$ . where q is specific humidity,  $\omega$  is vertical velocity,  $V_h$  is horizontal wind vector, res is the residual. The symbol  $<>=-\frac{1}{g}\int_{p_s}^0\cdot dp$  denotes a mass vertical integration through the entire atmosphere.

Denoting  $\delta$  as representing the trend form 1901–2020, and neglecting the submonthly transient eddies, the changes of the vertical moisture advection and horizontal moisture advection can be further divided into three terms:

$$-\delta \langle \omega \partial_p q \rangle = -\langle \overline{\omega_{cli}} \partial_p \delta \overline{q} \rangle - \langle \delta \overline{\omega} \partial_p \overline{q_{cli}} \rangle - \langle \delta \overline{\omega} \partial_p \delta \overline{q} \rangle \tag{2}$$

$$-\delta \langle V_h \cdot \nabla_h q \rangle = -\langle \overline{V_{h-cli}} \cdot \nabla \delta \overline{q} \rangle - \langle \delta \overline{V_h} \cdot \nabla \overline{q_{cli}} \rangle - \langle \delta \overline{V_h} \cdot \nabla \delta \overline{q} \rangle$$
 (3)

where overbars (·) indicate the monthly mean flow, and the

 $\overline{q_{cli}}$ ,  $\overline{V_{h-cli}}$  and  $\overline{\omega_{cli}}$  are the climatological mean monthly values of specific humidity, horizontal velocity and vertical velocity, respectively. The first term on the right-hand side of Eqs. (2) and (3) is associated with the thermodynamic component ( $\delta$ TH) induced by monthly specific humidity anomalies, the second term denotes dynamic component ( $\delta$ DY) induced by monthly horizontal/vertical wind anomalies, and the last term is defined as the nonlinear component ( $\delta$ NL) induced by monthly specific humidity anomalies and horizontal/vertical wind anomalies (Jin et al. 2020). Consequently, the yearly P trend ( $\delta$ P) can be decomposed as follows:

$$\delta P - \delta E = -\delta \langle V_h \cdot \nabla_h q \rangle - \delta \langle \omega \partial_p q \rangle + res \tag{4}$$



To investigate the combined effects of external forcing and internal variability on precipitation in NA, we analyzed observational datasets spanning the period from 1901 to 2020. Results indicate that decadal precipitation variability over NA is primarily characterized by two dominant modes. The first mode exhibits a consistent pattern of precipitation variability across NA (Fig. 1a and Extended Data Fig. 1a), with the corresponding time series showing an upward trend from 1901 to 2020 (Fig. 1b and Extended Data Fig. 1b), indicating a general increase in precipitation over the past century. The second mode exhibits a tripolar precipitation pattern extending from northeast to southwest (Fig. 1c and Extended Data Fig. 1c). Precipitation across northeastern Canada and the southwestern United States exhibits out-ofphase changes relative to western Canada and its southern region. The corresponding time series features pronounced decadal oscillations throughout the twentieth century (Fig. 1d and Extended Data Fig. 1d), rising in Period 2 and declining during Periods 1 and 3.

The long-term trend in observational data indicates a general wetting trend across NA (Fig. 2a, b). From 1901 to 2020, the annual mean precipitation across NA has increased notably, with a trend of 0.37 mm per month per decade (Fig. 2c, p < 0.01). To assess the relative contributions of the different external forcing to this observed wetting, we applied an optimal fingerprinting method to individual forcing simulations. The results indicate that NA is more likely to become wetter under both ALL and ANT forcing, with GHG forcing showing a greater probability and more members, suggesting that greenhouse gases play a significant role in the observed humidification of NA (Fig. 2c). However, NAT forcing does not exhibit a significant trend toward either wetting or drying, AA forcing is more likely to reduce precipitation in NA (Fig. 2c). The results of the optimal fingerprinting method also support these findings. Scaling factors (β) greater than zero were observed for ALL, ANT, and GHG forcing, whereas simulations with NAT and AA forcing could not account for the observed wetting in NA (Figs. 2d and 3c, e). Both ALL and ANT forcing underestimated the observed wetting (Figs. 2c and 3a, b). The GHG simulations closely match the observations (Figs. 2c and 3d). However, AA forcing can offset the precipitation increase induced by GHG forcing (Fig. 3b, d, e). The first mode is jointly influenced by greenhouse gases and aerosols, and we refer to this precipitation pattern as the external forcing precipitation pattern (Fig. 1a, b).

Although the external forcing precipitation pattern is primarily driven by GHG forcing, the positive trends of precipitation over NA are spatially non-uniform. Precipitation



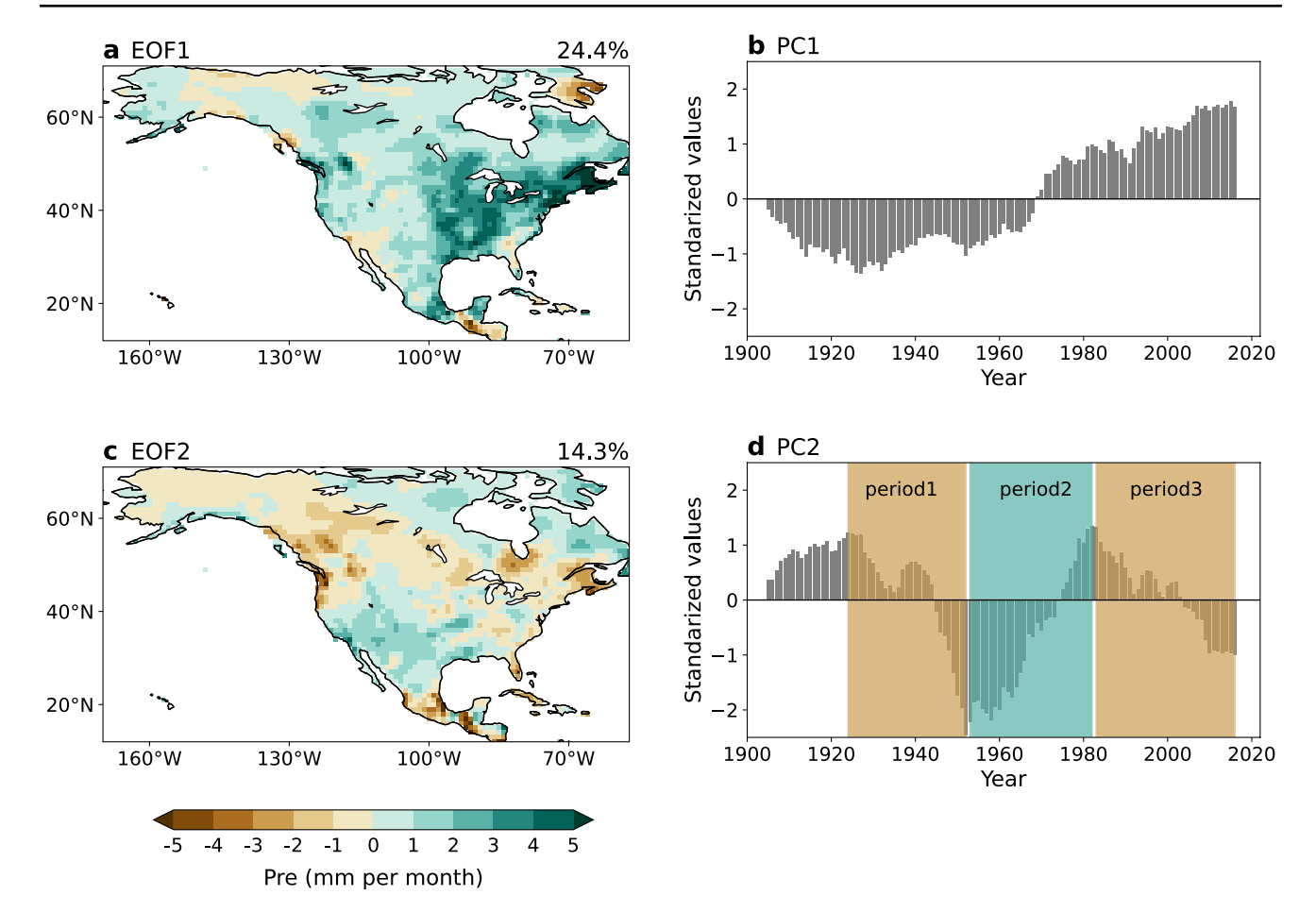


Fig. 1 The two leading modes of precipitation variations over NA at a decadal time scale. **a**, **c**, The first (**a**) and second (**c**) leading modes of the EOF analysis of NA annual precipitation derived from the CRU. **b**, **d**, The corresponding time series of the first and second precipitation patterns. Percentages in (**a**) and (**c**) denote the corresponding

explained variances. The yellow shading in (d) represents the periods of decreased precipitation (period 1: 1924–1952 and period 3: 1983–2016), while the green shading highlights the increased precipitation during period 2 (1953–1982)

decreases over southwestern NA but increases in other regions (Fig. 3d; Extended Data Fig. 3a, b). To investigate this uneven precipitation pattern under GHG forcing, we employ a land surface water budget analysis as described in the Methods. The area-averaged trend responses of the moisture budget terms to GHG forcing are shown in Extended Data Fig. 3c, d. The increase in precipitation of northern NA is dominated by increasing trends of the vertical and horizontal dynamic components. The vertical dynamic and horizontal components lead to precipitation decreases in the southwestern NA. The horizontal dynamic component provides an important background for the increase in precipitation of northern NA, which is characterized by wet advection from south to north (Extended Data Fig. 4a, b). The horizontal thermodynamic component causes decreased moisture from land to ocean over NA, creating a land-sea moisture gradient opposite to the wind field and leading to reduced precipitation in both western and eastern NA (Extended Data Fig. 4c, d). Despite the positive changes

in both the climatology and long-term trend of specific humidity driven by climate warming (Easterling et al. 2017; Prein et al. 2017; Zhang et al. 2024), precipitation changes driven by vertical moisture transport are determined by vertical velocity, whose spatial variations result in an uneven distribution of precipitation changes across NA (Extended Data Fig. 4e-h).

# 4 Mechanisms of internal variability modulating decadal precipitation changes

Precipitation over NA exhibits complex spatial and temporal oscillations on a decadal scale. The second precipitation mode (Fig. 1c, d) drives decadal variations in observed precipitation across NA. Periods 1 and 3 show similar precipitation trends, but they clearly differ from Period 2 (Fig. 4a-f). Specifically, during Periods 1 and 3, precipitation decreases in northeastern Canada and the southwestern



429 Page 6 of 15 X. Fan et al.

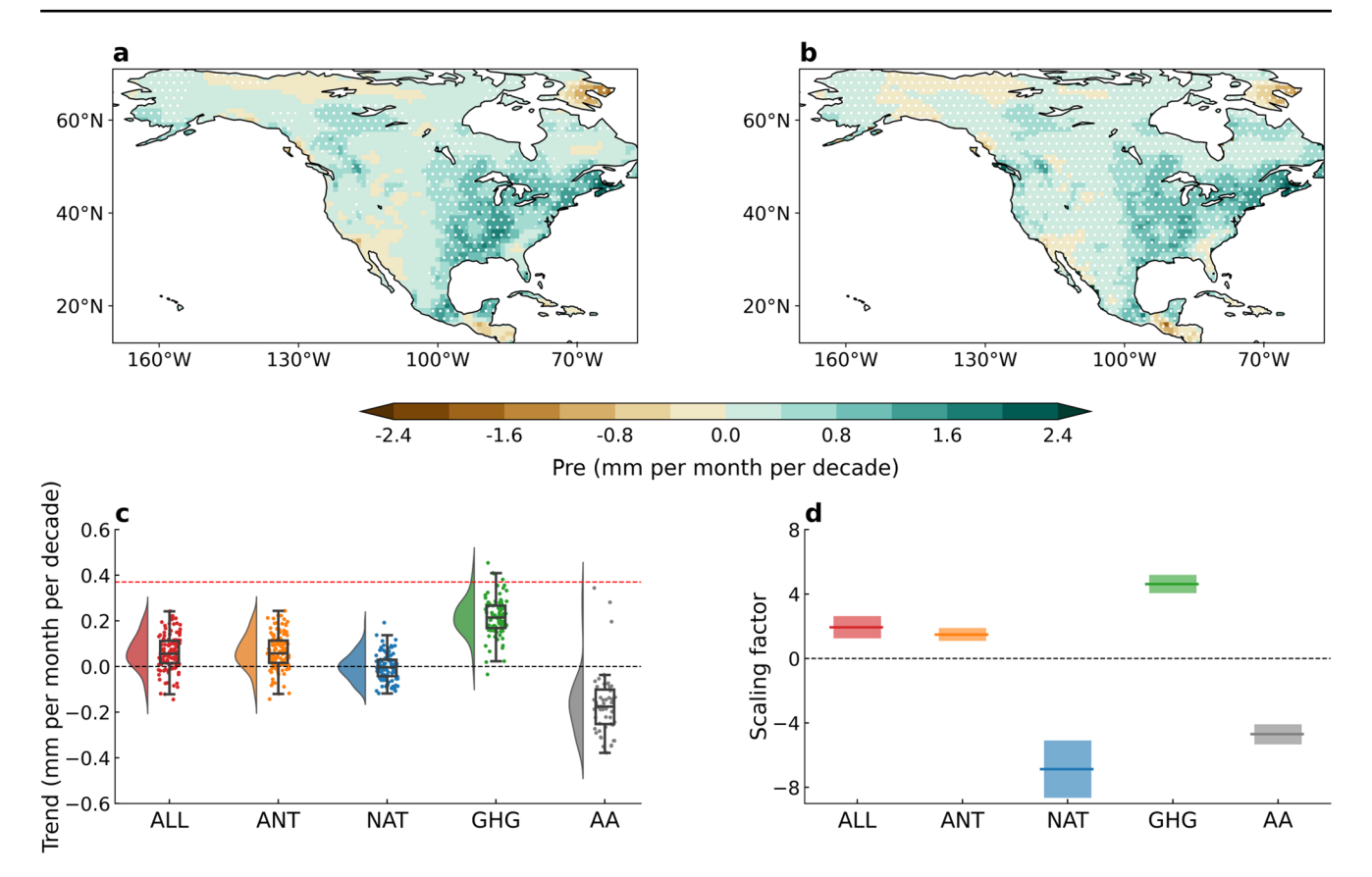


**Fig. 2** Externally forced changes in precipitation over NA. **a** The linear trend of the precipitation from 1901 to 2020 derived from the CRU. The stippling indicates significant trends at the 95% (P<0.05) confidence level. **b** The linear trend of the first precipitation pattern over NA derived from EOF1×PC1<sub>trend</sub> (Fig. 1a, b). **c** The linear trends of the annual mean precipitation across NA of the single forcing precipitation pattern from 1901 to 2020 under ALL (red), ANT (yellow), NAT (blue), GHG (green), and AA (grey) forcing derived from all the members of the 10 CMIP6 models. The red dash line shows the linear trend of the annual mean precipitation across NA derived from CRU. A positive trend denotes a wetting tendency over NA. Box and whisker

United States and Mexico. While the spatial distribution of precipitation enhancement differs between the two periods, both epochs exhibit a tripolar pattern across the northeastsouthwest (Fig. 4a, c). The precipitation trend during Period 2 aligns with the second precipitation mode (Fig. 1c), except for some differences over eastern NA (Fig. 4b). The reconstructed precipitation from the first and second modes indicates that decadal precipitation is jointly modulated by both modes (Fig. 4a-f). The relative contributions of the first and second modes in the four key regions (black boxes in Fig. 4d) during the three periods suggest that the second mode exerts a stronger modulation on decadal timescales than the first mode. Furthermore, depending on its phase, the second mode can either enhance or offset the NA wetting associated with the first mode during periods 1–3 (Fig. 4gi). Although the precipitation increase over NA during the past century is primarily driven by the first mode (Fig. 1a,

plots show the 5th, 25th, 50th, 75th and 95th percentiles of all members (n=125, 125, 100, 93 and 53 for ALL, ANT, NAT, GHG and AA forcing, respectively). The lines denote the kernel estimate of the probability density function of the trends using 100 bins. The dot represents the distribution of individual members. **d** Optimal fingerprint detection and attribution analysis (Methods) on the changes in the single forcing precipitation pattern over NA from 1901 to 2020. The lines denote the scaling factors of one-signal analysis for simulations under ALL, ANT, NAT, GHG and AA forcing, respectively. Error bars denote the corresponding 90% confidence intervals

b), the trends in decadal precipitation are primarily driven by decadal variability (Fig. 1c, d). We will further explore the underlying mechanisms responsible for the second precipitation mode.

The positive phase of the IPO is typically characterized by positive SST anomalies in the tropical central-eastern Pacific and negative anomalies in the northern Pacific (Extended Data Fig. 2a). The positive phase of the AMO is often associated with anomalously warm SST in the North Atlantic Ocean (Extended Data Fig. 2c). Over the past century, these two signals exhibited significant oscillation (Extended Data Fig. 2b, d). However, the relative contributions and underlying mechanisms of low-frequency signals from the Pacific and Atlantic to the second precipitation mode over NA remain unclear. Therefore, we analyze SST change from both observational data and CMIP6 simulations for the period 1901–2020. The observed SST change is



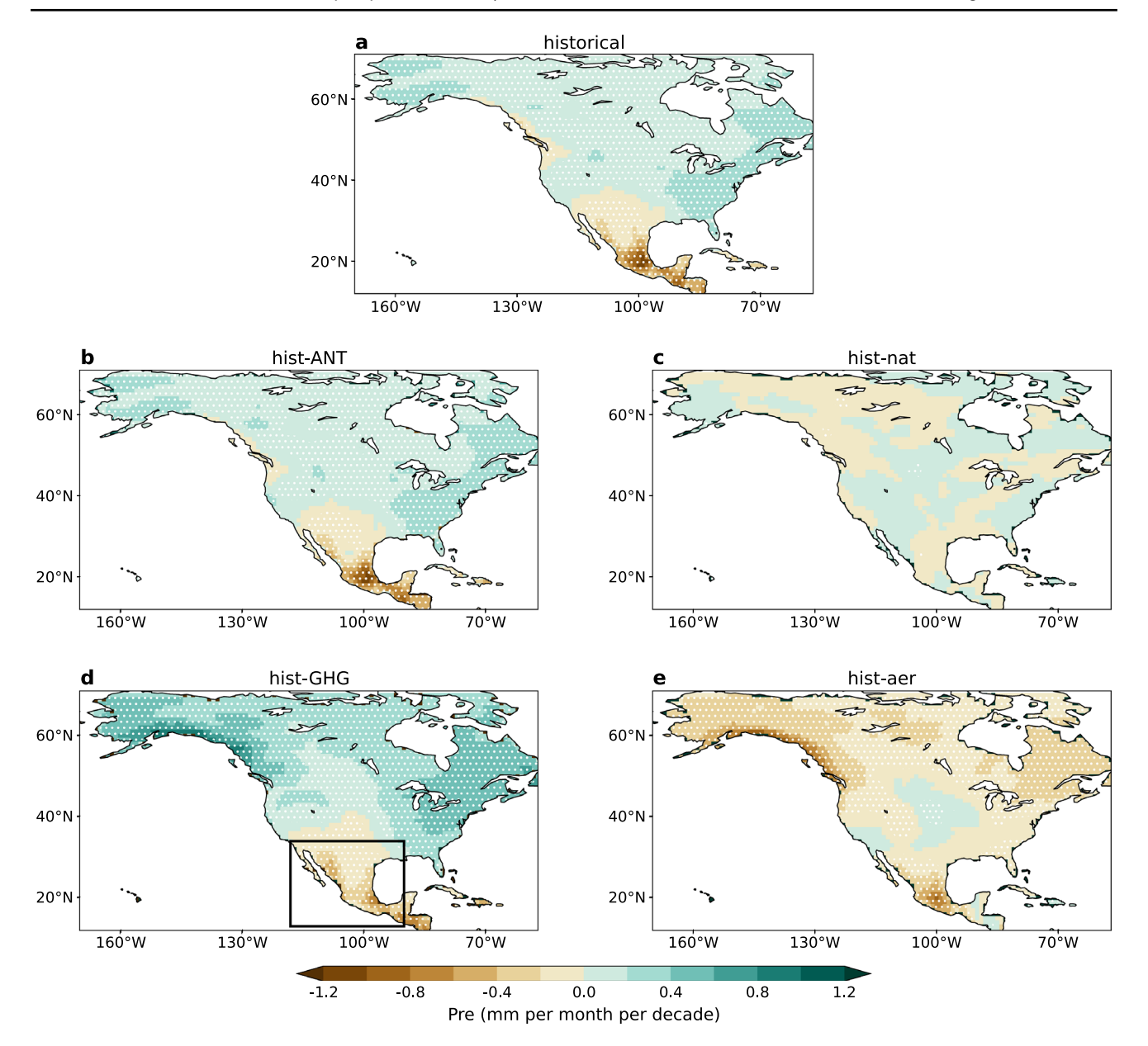


**Fig. 3** Long-term changes in precipitation over NA under different external forcing. **a**–**e** The linear trends of precipitation from 1901 to 2020 under ALL (**a**), ANT (**b**), NAT (**c**), GHG (**d**) and AA (e) forcing derived from the multimodel average of 10 CMIP6 models. The

domains (13–34°N, 90–118°W) in southern NA experiencing reduced precipitation are indicated by boxes in (d). The stippling indicates significant trends at the 95% (P<0.05) confidence level

characterized by a positive-IPO-like pattern (Fig. 5b), while a negative-AMO-like pattern in the North Atlantic (Fig. 5b). The synchronous variation in the second precipitation mode and decadal SST change strongly suggests the influence of internal variability (Fig. 5b). We refer to it as the internal variability precipitation pattern (Fig. 1c, d). The internal variability precipitation pattern (Fig. 1d) shows a strong positive correlation with the IPO index (0.66 cor with PC2, p<0.01) and a weak negative correlation with the AMO index (-0.25 cor with PC2, p<0.01).

Further exploring which internal variability plays a pivotal role in the generation of internal variability precipitation pattern, we utilize a large ensemble of 90 model members, derived from the ACCESS-ESM1-5 and MIROC6 models, which stand out for their large number of realizations among the 10 CMIP6 models. We focus on two sub-ensembles, each containing the 10 extreme members with the maximum and minimum precipitation patterns, respectively (hereafter "MAX10" and "MIN10"). We calculate the precipitation change difference of sub-ensemble mean between the MAX10 and MIN10 members, which resembles the



429 Page 8 of 15 X. Fan et al.

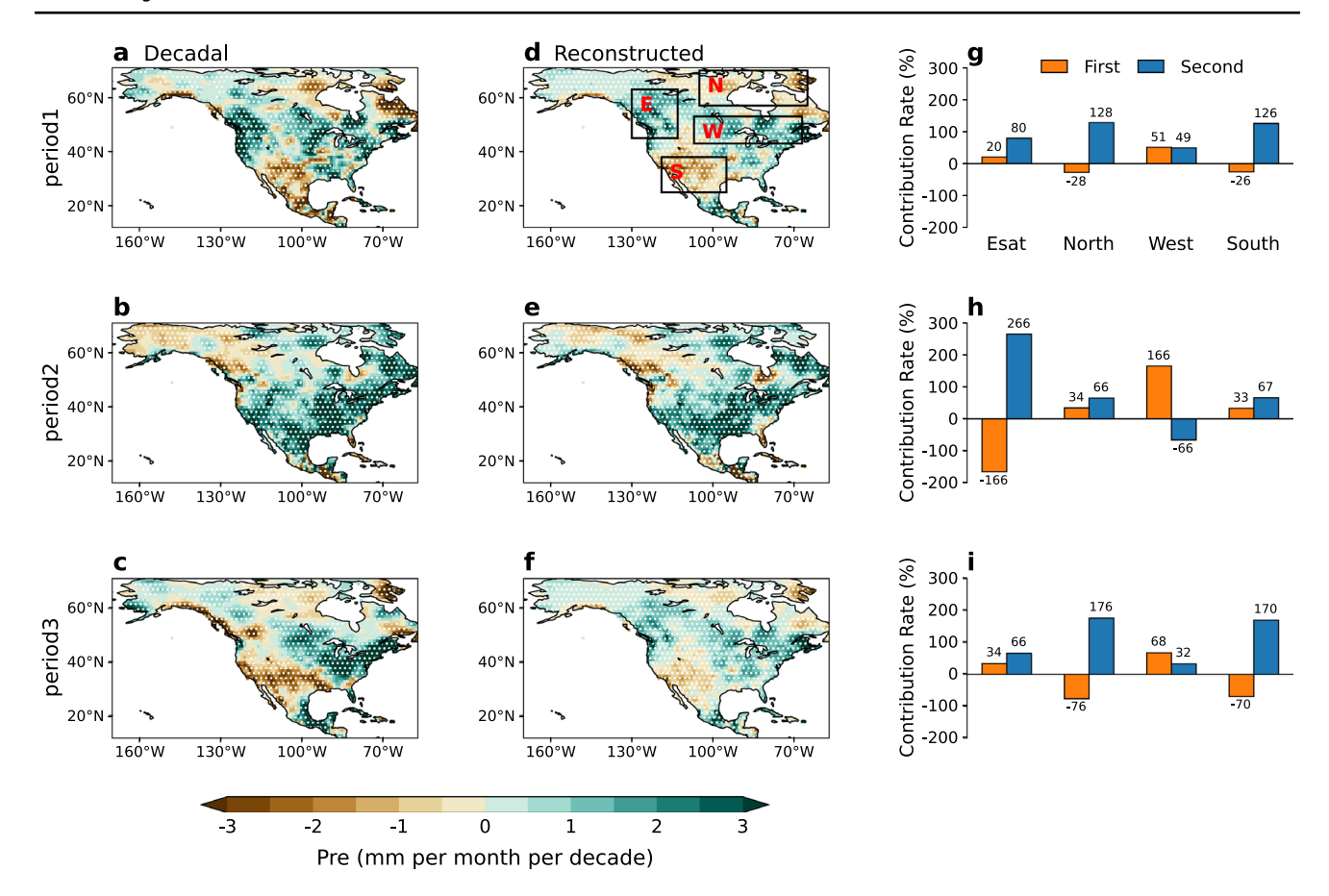


**Fig. 4** The second pattern modulated precipitation trend on a decadal scale. **a**, **b**, **c** The linear trends of decadal precipitation over NA derived from the CRU for periods 1–3 (Fig. 1d). The precipitation decadal component—that is the 9-year running mean performed after de-trending the raw data. **d**, **e**, **f** are the same as **a**, **b**, **c** but for precipitation reconstructed from the first and second precipitation modes. The stippling indicates significant trends at the 95% (P<0.05)

confidence level. The reconstructed precipitation expressed as: P=EOF1×PC1+EOF2×PC2. **g**, **h**, **i** the relative contribution of first and second modes for four regions as show in **d** (East: 45–63°N, 113–130°W, North: 57–70°N, 65–105°W, West: 43–53°N, 67–107°W, South: 25–38°N, 95–119°W) during periods 1–3. The numbers indicate the first and second mode relative contribution rate, which is calculated by (EOF1×PC1)/P and (EOF2×PC2)/P, respectively

internal variability precipitation pattern (Fig. 5a, c). The SST difference between the sub-ensemble mean reflects a positive IPO-like pattern, while the AMO shows no significant correlation (Fig. 5d). Furthermore, we assess the modulation of the internal variability precipitation pattern by the IPO and AMO across the 90-member ensemble. A notable positive correlation is found between internal variability precipitation and the IPO (Fig. 5e), whereas the AMO does not exhibit a pronounced negative correlation (Fig. 5f). In addition, when models skillfully simulate the IPO, they reproduce similar internal variability precipitation pattern (Extended Data Fig. 5). Therefore, observations and the large-ensemble simulations highlight the dominant role of the IPO in shaping the internal variability of precipitation over NA. The spatial variation trend of NA precipitation on decadal scales is modulated by the phase transition of the IPO.

To clarify the dynamical mechanisms of the internal variability precipitation pattern driven by the IPO, the eddy

stream function (Esf) and Plumb wave activity flux (Paf) were used to analyze the stationary Rossby wave trains. Sea surface temperature anomalies associated with the IPO trigger large-scale Rossby waves that propagate downstream from the North Pacific across NA to Greenland, ultimately reaching the North Atlantic basin (Fig. 6a). This propagation pattern exhibits remarkable similarity to the PNA teleconnection pattern (Wallace and Gutzler 1981), characterized by the concurrent development of low-pressure systems over the northern Pacific Ocean, Greenland, and southern NA, while pronounced high-pressure centers form over the northern NA sector and central North Atlantic basin (Fig. 6b). The well-developed anticyclonic circulation regime persists over northern NA, resulting in reduced water vapor flux and prevailing subsidence (Fig. 6c, d). Moisture from the eastern tropical Pacific and the Gulf of Mexico accumulates over southern NA, where persistent low-pressure systems allow moisture to rise in the region. Additionally, the low pressure over Greenland also creates favorable



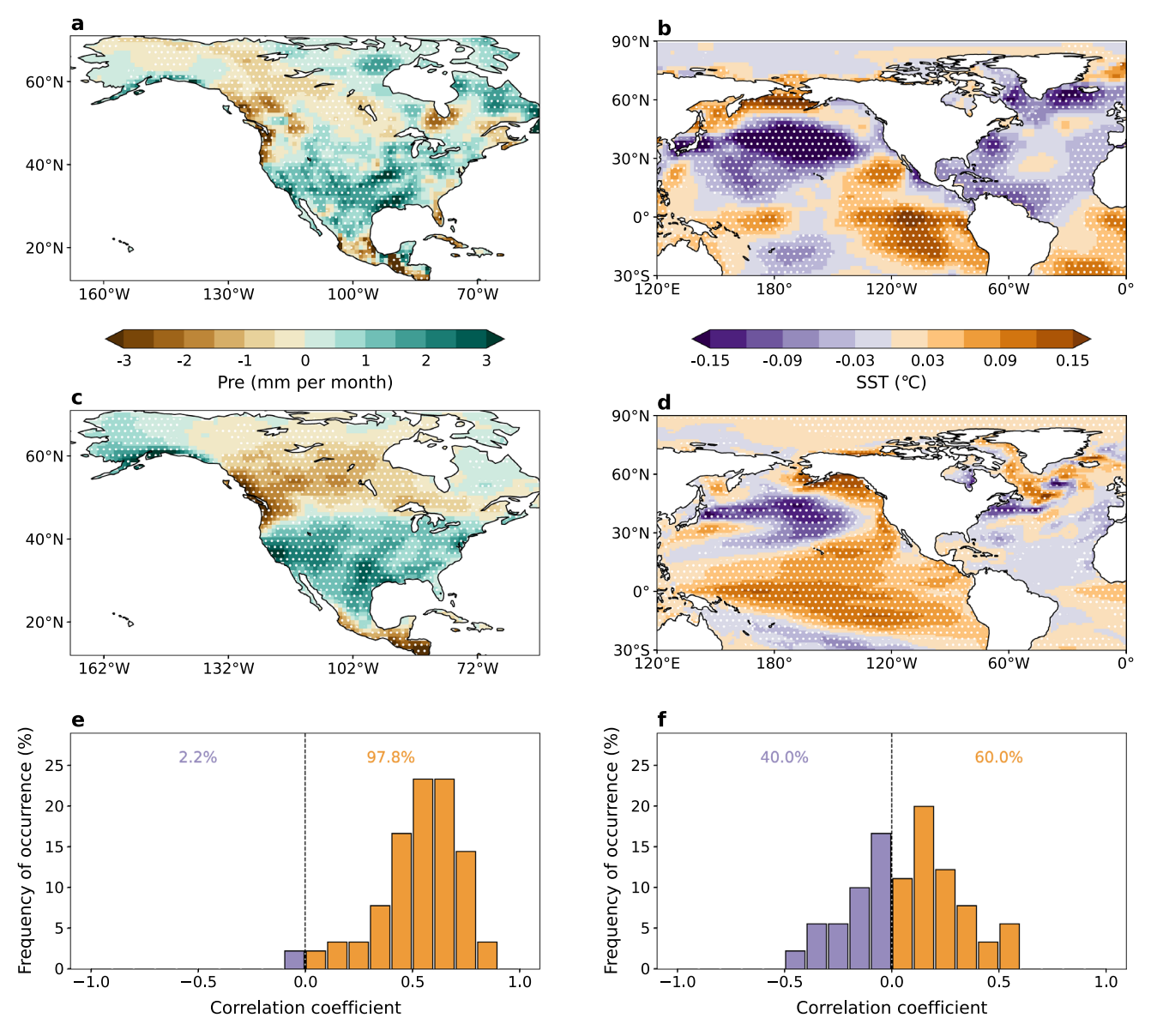


**Fig. 5** IPO-dominated changes related to internal variability precipitation pattern over NA. **a**, **b** The decadal component of precipitation derived from the CRU (**a**) and SST derived from the ERSST (**b**) regressed onto the corresponding time series of the internal variability precipitation pattern from 1901 to 2020 (Fig. 1d, bar). **c**, **d** are the same as **a**, **b** but for model simulated decadal component (difference between MAX10 and MIN10) regressed onto the corresponding model simulated time series (difference between MAX10 and MIN10) of the internal variability precipitation pattern from 1901 to 2020 derived from all members of ACCESS-ESM1-5 and MIROC6 (n=90). The model simulated time series was calculated by regressing the simulated precipitation over NA onto the internal variability precipitation pattern derived from the CRU (Fig. 1c). The MAX10 denotes the 10

members that best simulate internal variability precipitation (The top 10 of 90 correlation coefficients that model simulated time series and the CRU time series (Fig. 1d, bar)). MIN10 is the opposite of MAX10. The stippling indicates significant correlations at the 95% (P<0.05) confidence level.  $\bf e$ , Histograms for the correlation coefficients between the corresponding time series of the internal variability precipitation pattern and IPO index derived from all members of ACCESS-ESM1-5 and MIROC6 (n=90); the width of each histogram is 0.1; the numbers denote the percentages of members with negative or positive correlation coefficients.  $\bf f$  is the same as  $\bf e$ , but for the correlation coefficients between the corresponding time series of the internal variability precipitation pattern and AMO index



429 Page 10 of 15 X. Fan et al.

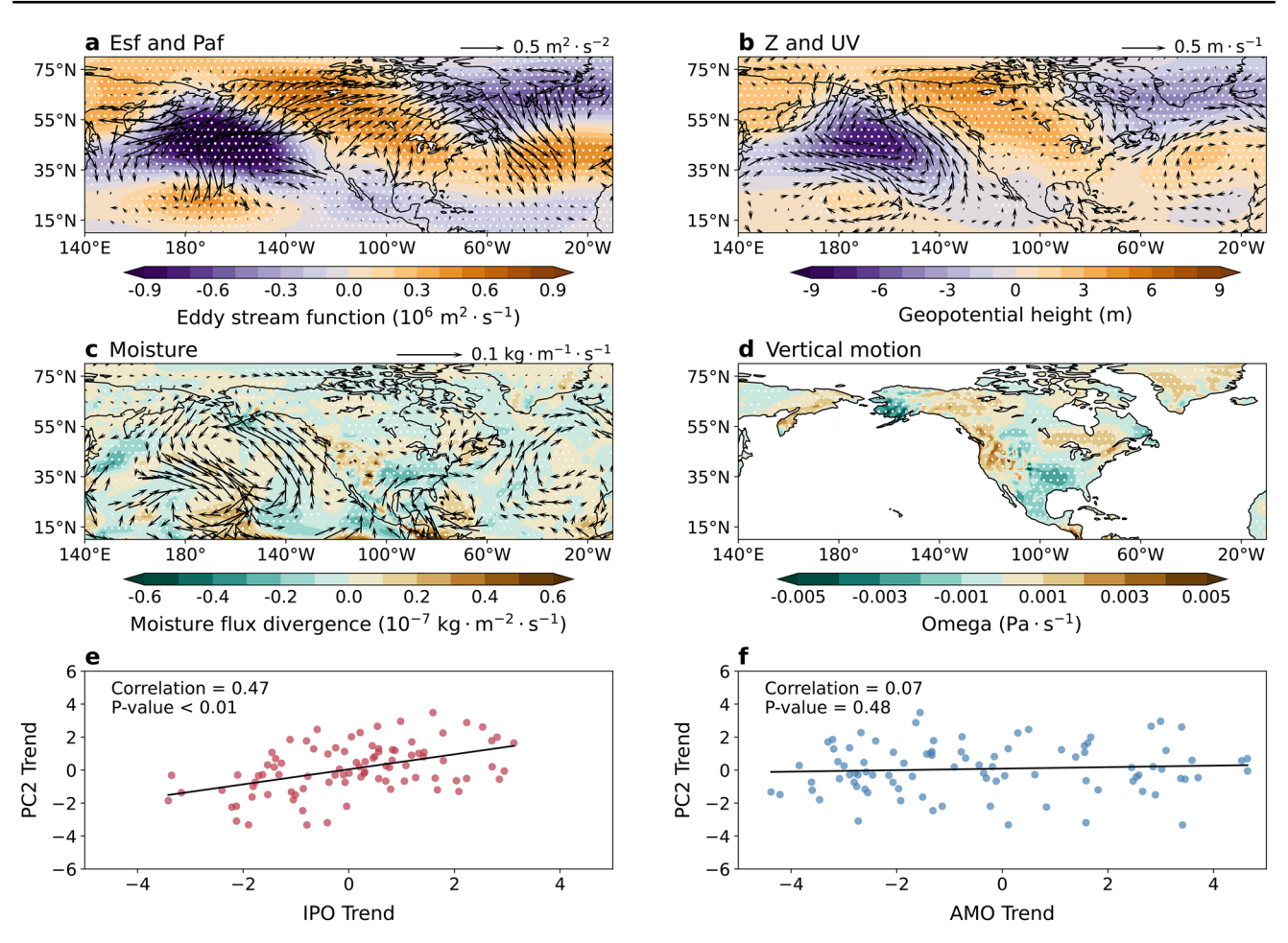


Fig. 6 The mechanisms of internal variability's influence on precipitation pattern over NA. **a**–**d** The decadal component of Eddy stream function (shading) and Plumb wave activity flux (vector) at 500 hPa **a** 500-hPa geopotential height Z (shading) and 850-hPa wind (UV) **b** column-integrated moisture divergence (shading) and moisture flux (vectors) **c** and **d** 500-hPa vertical velocity regressed onto the corresponding time series of internal variability precipitation pattern (Fig. 1d, bar). The stippling indicates significant correlations at the

95% (P<0.05) confidence level. The vectors are shown only when the zonal or meridional component is significant at the 95% confidence level. The above analysis is based on reanalysis data.  $\bf e$  Shows scatter plots between the corresponding time series of the internal variability precipitation pattern trends and the IPO trends during the period 3, where the black lines show the regression of data points for 90 members of ACCESS-ESM1-5 and MIROC6.  $\bf f$  is the same as  $\bf e$ , but for the internal variability precipitation trends and AMO trends

conditions for increased precipitation over northeastern NA (Fig. 6b-d). These circulation patterns ultimately lead to the formation of the internal variability precipitation pattern shown in Fig. 5a. The recent change in precipitation trends during period 3 (Fig. 4c, f) is associated with the negative phase shift of the IPO (Extended Data Fig. 2b). This shift is clearly linked to the IPO rather than the AMO (Fig. 6e, f).

# 5 Decadal and long-term projections of precipitation over NA

Although past greenhouse gas emissions have contributed to an overall increase in precipitation across NA, the IPO exerts a significant influence on the spatial patterns of NA precipitation at decadal scale. However, considerable

uncertainty exists among different model members due to internal variability (Fig. 7a). The difference of sub-ensemble mean between the MAX10 and MIN10 is highly consistent with observational data (Fig. 7a), which means that largeensemble simulations can adequately capture the observed internal variability precipitation pattern. To further investigate future precipitation trend, we conducted composite analyses for the 2021-2050 period under the RCP4.5 scenario, the precipitation trend between MAX10 and MIN10 shows an increase trend, while the MIN10-MAX10 difference exhibits a decrease trend (Fig. 7a). The internal variability precipitation pattern exhibits a tripolar wet-dry-wet structure from north to south (Fig. 7b). The SST trend resembles a positive IPO-like pattern, with warming in the central-eastern equatorial Pacific (Fig. 7c). In contrast, external forcing induces overall ocean warming, leading to



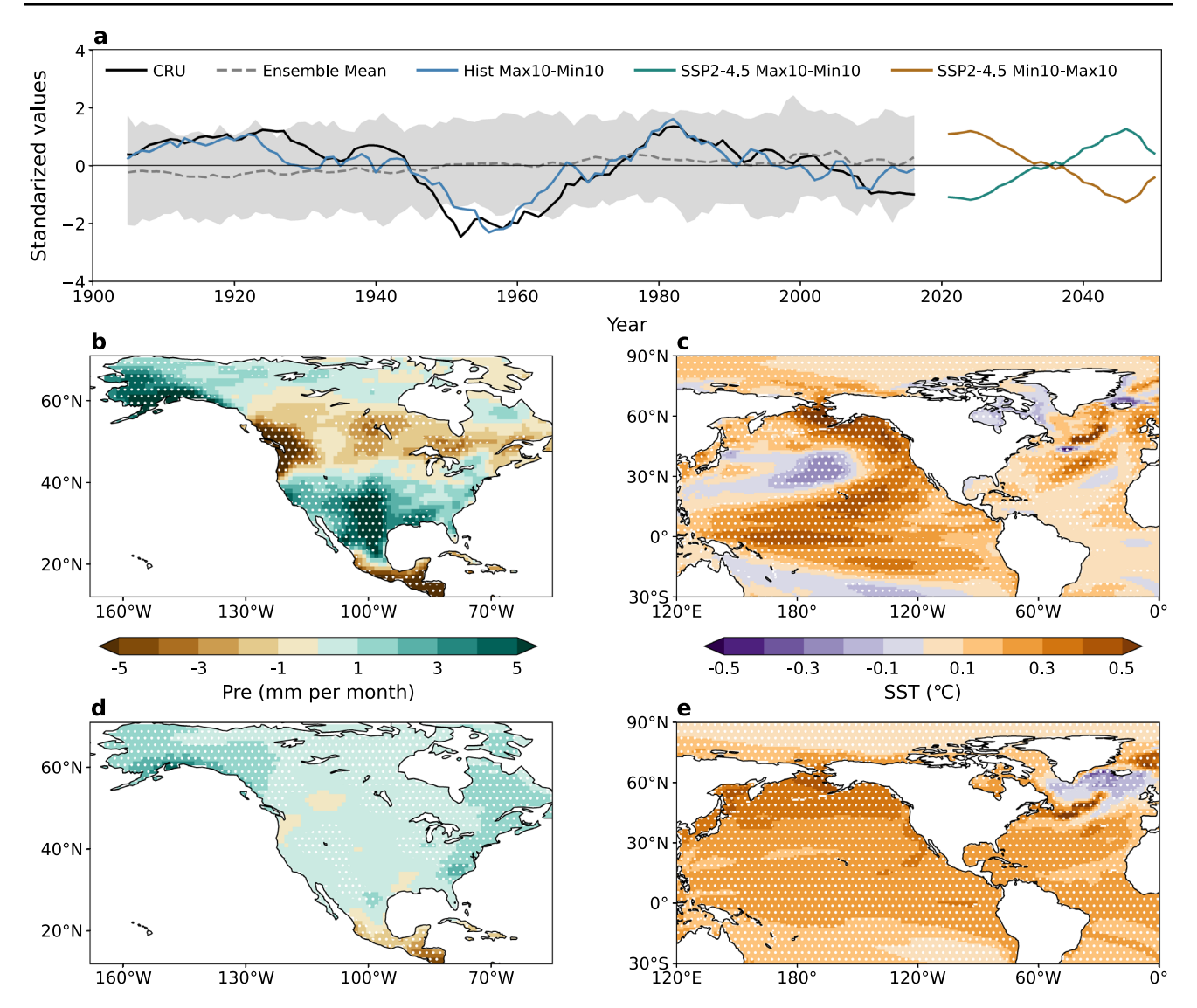


**Fig. 7** Projected NA precipitation change and associated SST trend in the near future. **a** Time series of internal variability precipitation patterns from CRU (black line) and model ensemble mean and MAX10-MIN10 under historical period (gray dash line and blue line, 1901–2020) and future SSP2-4.5 scenario MAX10-MIN10 and MIN10-MAX10 (green and brown line) during the period of 2021–2050, the gray shading denotes the 95% model intervals. **b**, **c** Spatial

patterns of ensemble mean of precipitation (b) and SST (c) trend difference between MAX10 and MIN10 during 2021–2050. **d, e** Spatial pattern of (d) ensemble mean of precipitation trend and (e) SST trend during the period of 2021–2050 from 10 models under the SSP2-4.5. The stippling indicates significant trends at the 95% (P<0.05) confidence level

increased precipitation across NA (Fig. 7d, e). However, the overall wetting of NA caused by external forcing is smaller than the precipitation changes associated with internal variability driven by the positive phase shift of the IPO (Fig. 7b, d). Therefore, the IPO plays a crucial role in the decadal trend of future precipitation over NA. Reducing the uncertainty in IPO prediction will enhance the near-term projection of NA precipitation.

As demonstrated by our previous findings, both ALL and ANT forcing significantly underestimate historical precipitation change in NA (Fig. 3a, b). In contrast, GHG forcing effectively simulates the long-term precipitation trends in

the region, although it slightly underestimates both the spatial distribution and the magnitude of the trend (Fig. 3d). For the region average of NA precipitation (Extended Data Fig. 6), the observed long-term trend is 0.37 mm per month per decade (p<0.01). The trends under different forcing are as follows: ALL forcing (0.06 mm per month per decade for 10 models, 0.07 mm for MIROC6, p<0.01), ANT forcing (0.06 mm per month per decade for 10 models, 0.08 mm for MIROC6, p<0.01), and GHG forcing (0.22 mm per month per decade for 10 models, 0.20 mm for MIROC6, p<0.01). The main reason for the differences in precipitation trend among ALL, ANT, and GHG forcing in NA is



429 Page 12 of 15 X. Fan et al.

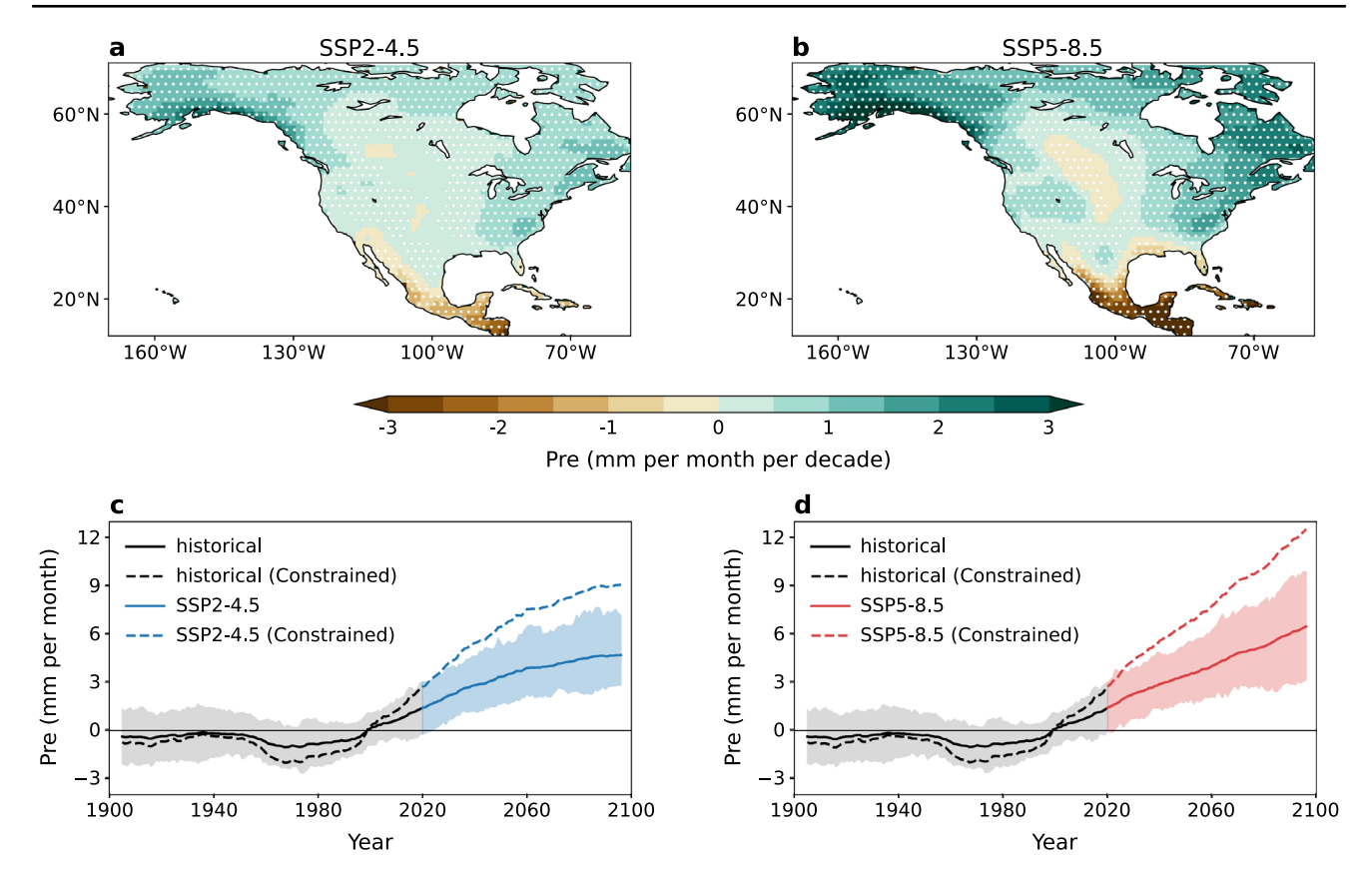


**Fig. 8** Future changes in precipitation over NA associated with externally forced changes. The linear trends of precipitation under the SSP2-4.5 **a** and SSP5-8.5 **b** scenarios from 2021–2100 derived from the multimodel average of 10 CMIP6 models. The stippling indicates significant trends at the 95% (*P*<0.05) confidence level. **c** Annual mean precipitation anomalies over the NA (relative to 1985–2014) during 1901–2100 in the CMIP6 multimodel historical simulations

and future SSP2-4.5 scenario. The solid curves indicate the multimodel ensemble means and the shading denotes the 95% model intervals, derived from the raw model output. The dashed curves indicate the constrained projections by multiplying the ensemble mean projections with the scaling factor of ALL forcing from Fig. 2d. **d** is the same as c but for future SSP5-8.5 scenario

the significant discrepancy in simulations prior to the 1970s. After the 1970s, the precipitation reduction induced by aerosols diminishes (Extended Data Fig. 6).

The CMIP6 multimodel ensemble mean indicates a significant long-term wetting trend over most of NA under both the SSP2-4.5 and SSP5-8.5 scenarios (Fig. 8a, b and Extended Data Fig. 7). Under the SSP2-4.5 scenario, simulations with the MIROC6 model driven by the respective forcing also confirm an increase in precipitation over NA due to GHG forcing, the aerosols also showed a positive effect (Extended Data Fig. 8). The ALL forcing simulation shows improved consistency with precipitation observations after 1970, due to the inclusion of both aerosol and greenhouse gas effects (Extended Data Fig. 6), it is assumed that it remains a reasonable representation for future projections. To constrain future projections, the scaling factor derived from the attribution results for ALL forcing (Fig. 2d) is applied to the ensemble mean precipitation responses under the SSP2-4.5 and SSP5-8.5 scenarios. The constrained results indicate that NA will become wetter under both the SSP2-4.5 and SSP5-8.5 scenarios (Fig. 8c, d).

#### 6 Conclusion and discussion

In this study, we explore the combined effects of external forcing and internal variability on NA precipitation. Our results reveal two distinct precipitation patterns over the past century using long-term observational data and CMIP6 model simulations: the external forcing precipitation pattern, characterized by a general wetting trend, and the internal variability precipitation pattern, marked by significant decadal oscillation. Optimal fingerprinting analysis of data from 1901 to 2020 shows that the wetting trend in NA is primarily driven by greenhouse gas emissions. However, state-of-the-art climate models tend to underestimate the influence of external forcing on NA precipitation, particularly under ALL and ANT forcing. In contrast, GHG forcing aligns more closely with observed trends despite being



slightly underestimated. The underestimation of ALL and ANT forcing over NA is largely because AA forcing can offset the precipitation increase induced by GHG forcing (Extended Data Fig. 6). Aerosols influence precipitation through both large-scale atmospheric circulation adjustments (macro-scale) and microphysical aerosol-cloud interactions, with their combined effects mediated by complex feedback mechanisms (Tao et al. 2012; Li et al. 2019; Jiang et al. 2023; Zhao et al. 2025). Previous studies indicated a significant shift in aerosol emissions over the NA around the 1970s (Risser et al. 2024; Jiang et al. 2025), which may have contributed to changes in regional precipitation patterns.

In addition to the long-term wetting driven by external forcing, internal variability significantly influences NA precipitation through decadal oscillations. This modulation is significantly more prominent than the external forcing on a decadal time scale, generating a tripolar precipitation pattern pronounced during three distinct historical periods. Climate model simulations confirm that the impact of the AMO on NA precipitation is significantly weaker than that of the IPO. The phase transitions of the IPO predominantly govern the tripolar internal variability precipitation pattern. Sea surface temperature anomalies associated with the IPO trigger large-scale Rossby waves. The wave train originating from the Pacific propagates downstream, influencing atmospheric circulation and moisture transport, ultimately shaping the tripolar precipitation pattern observed in NA. Finally, future decadal and long-term trends in NA precipitation are projected using CMIP6 climate models. Results suggest that from 2021 to 2050, NA precipitation may continue to exhibit the tripolar pattern, depending on the phase transition of the IPO. This underscores the importance of early predictions of the IPO phase to enhance near-term precipitation forecasts in NA. When constraining future projections with the optimal fingerprinting method, we find that under both the SSP2-4.5 and SSP5-8.5 scenarios, greenhouse gases and aerosols will continue to drive the prevailing wetting trend in NA.

Although our study provides a comprehensive attribution of long-term precipitation changes over NA, identifying GHG-induced long-term wetting and IPO-driven decadal oscillations, and elucidating the mechanisms by which the IPO influences these decadal precipitation variations, it still has some limitations. Notably, historical observations indicate a wetting trend in the Mexico region (Fig. 2a, b), whereas model simulations reveal a robust drying trend that persists across both historical and future scenarios under GHG forcing (Extended Data Fig. 3 and Extended Data Fig. 8d). This discrepancy in regional climate simulations merits further investigation. Additionally, we emphasize that phase shifts in the IPO significantly impact NA precipitation patterns over the next 30 years, making accurate IPO

predictions crucial for future climate projections (Huang et al. 2020; Wu et al. 2024). Such improvements could substantially enhance the reliability of near-term precipitation forecasts for NA.

These findings have broad implications for climate prediction and adaptation, highlighting the critical role of interactions between external forcing and internal variability in shaping precipitation patterns. Our research provides valuable insights into the interplay between human-induced climate change and natural climate variability, contributing to the ongoing study of climate change impacts and strategies for mitigation.

**Supplementary Information** The online version contains supplementary material available at https://doi.org/10.1007/s00382-025-07937-9.

**Acknowledgments** We thank the anonymous reviewers for their constructive comments and helpful suggestions, which helped us to improve our paper.

**Author contributions** JH and YX contributed to the concept and design of the research. XF conducted the analysis and prepared the draft. All authors analyzed and discussed the results, commented on the manuscript, and contributed to the manuscript.

**Funding** This work was supported by the National Natural Science Foundation of China (41991231), the Fundamental Research Funds for the Central Universities (Izujbky-2025-jdzx01).

Data availability The CRU data are available from the CEDA Archive (https://crudata.uea.ac.uk/cru/data/hrg/). The GPCC data are available from the National Oceanic and Atmospheric Administration (NOAA) Physical Sciences Laboratory (https://psl.noaa.gov/data/gridded/data.gpcc.html). ERSSTv5 are available from (https://psl.noaa.gov/data/gridded/data.noaa.ersst.v5.html). The 20CRV3 reanalysis data are available from (https://psl.noaa.gov/data/gridded/data.20thC\_ReanV3.html). The NEP-DOE Reanalysis 2 form (https://psl.noaa.gov/data/gridded/data.ncep.reanalysis2.html). CMIP6 model simulations are available at (https://esgf-node.llnl.gov/search/cmip6/).

#### **Declarations**

**Conflict of interest** The authors have no relevant financial or non-financial interests to disclose.

Ethics approval and consent to participate Not applicable.

Consent for publication Not applicable.

## References

Agel L, Barlow M (2020) How well do CMIP6 historical runs match observed Northeast U.S. precipitation and extreme precipitation related circulation? J Climate 33(22):9835–9848. https://doi.org/ 10.1175/JCLI-D-19-1025.1



- Allen MR, Stott PA (2003) Estimating signal amplitudes in optimal fingerprinting, part I: theory. Clim Dyn 21(5):477–491. https://doi.org/10.1007/s00382-003-0313-9
- Allen MR, Tett SF (1999) Checking for model consistency in optimal fingerprinting. Clim Dyn 15(6):419–434. https://doi.org/10.1007/s003820050291
- Ault TR, George SS (2010) The magnitude of decadal and multi-decadal variability in North American precipitation. J Climate 23:842–850. https://doi.org/10.1175/2009JCLI3013.1
- Cai Q, Chen W, Chen S et al (2024) Recent pronounced warming on the Mongolian Plateau boosted by internal climate variability. Nat Geosci 17:181–188. https://doi.org/10.1038/s41561-024-01377-6
- Chen Z, Gan B, Wu L et al (2018) Pacifc-North American teleconnection and North Pacifc Oscillation: historical simulation and future projection in CMIP5 models. Clim Dyn 50:4379–4403. https://doi.org/10.1007/s00382-017-3881-9
- Chikamoto Y, Timmermann A, Widlansky MJ et al (2017) Multi-year predictability of climate, drought, and wildfire in southwestern North America. Sci Rep 7:6568. https://doi.org/10.1038/s41598-017-06869-7
- Chou C, Lan C (2012) Changes in the annual range of precipitation under global warming. J Climate 25(1):222–235. https://doi.org/10.1175/JCLI-D-11-00097.1
- Dai A (2013) The influence of the inter-decadal Pacific Oscillation on US precipitation during 1923–2010. Clim Dyn 41:633–646. https://doi.org/10.1007/s00382-012-1446-5
- Dong L, Leung LR (2022) Roles of external forcing and internal variability in precipitation changes of a sub-region of the U.S. mid-Atlantic during 1979–2019. J Geophys Res Atmos 127:e2022JD037493. https://doi.org/10.1029/2022JD037493
- Dong L, Leung LR, Song F et al (2021) Uncertainty in El Niño-like warming and California precipitation changes linked by the Inter-decadal Pacific Oscillation. Nat Commun 12:6484. https://doi.org/10.1038/s41467-021-26797-5
- Douville H, Ribes A, Decharme B et al (2013) Anthropogenic influence on multidecadal changes in reconstructed global evapotranspiration. Nat Clim Chang 3(1):59–62. https://doi.org/10.1038/nc limate1632
- Easterling DR, Kunkel KE, Arnold JR (2017) Precipitation change in the United States. In: Wuebbles DJ, Fahey DW, Hibbard KA (eds) Climate science special report: 4th national climate assessment vol I, U.S. Global Change Research Program, pp 207–230 https://doi.org/10.7930/J0H993CC
- Enfeld DB, Mestas-Nuñez AM, Trimble PJ (2001) The Atlantic Multidecadal oscillation and its relation to rainfall and river fows in the continental U.S. Geophys Res Lett 28:2077–2080. https://doi.org /10.1029/2000GL012745
- Feng S, Fu Q (2013) Expansion of global drylands under a warming climate. Atmos Chem Phys 13:10081–10094. https://doi.org/10.5 194/acp-13-10081-2013
- Grigg NS (2014) The 2011–2012 drought in the United States: new lessons from a record event. Int J Water Resour Dev 30(2):183–199. https://doi.org/10.1080/07900627.2013.847710
- Harris I, Jones PD, Osborn TJ et al (2014) Updated high-resolution grids of monthly climatic observations the CRU TS3.10 dataset. Int J Climatol 34:623–642. https://doi.org/10.1002/joc.3711
- Hayhoe K, Wake CP, Huntington TG et al (2007) Past and future changes in climate and hydrological indicators in the US Northeast. Clim Dyn 28:381–407. https://doi.org/10.1007/s00382-00 6-0187-8
- Held IM, Soden BJ (2006) Robust responses of the hydrological cycle to global warming. J Clim 19(21):5686–5699. https://doi.org/10 .1175/JCLI3990.1
- Hu Q, Feng S (2012) AMO- and ENSO-driven summertime circulation and precipitation variations in North America. J Climate 25:6477–6495. https://doi.org/10.1175/JCLI-D-11-00520.1

- Huang J, Yu H, Guan X et al (2016) Accelerated dryland expansion under climate change. Nat Clim Change 6:166–171. https://doi.org/10.1038/nclimate2837
- Huang X, Zhou T, Dai A et al (2020) South Asian summer monsoon projections constrained by the interdecadal Pacific oscillation. Sci Adv 6:eaay6546. https://doi.org/10.1126/sciadv.aay6546
- Huang H, Patricola CM, Winter JM et al (2021) Rise in Northeast US extreme precipitation caused by Atlantic variability and climate change. Weather Clim Extremes 33:100351
- Huang F, Xu Z, Guo W et al (2023) Relative contributions of internal variability and external forcing to the inter-decadal transition of climate patterns in East Asia. Npj Clim Atmos Sci 6:21. https://doi.org/10.1038/s41612-023-00351-0
- Jiang J, Zhou T, Qian Y et al (2023) Precipitation regime changes in High Mountain Asia driven by cleaner air. Nature 623:544–549. https://doi.org/10.1038/s41586-023-06619-y
- Jiang J, Zhou T, Zhang W (2025) Aerosol mitigation matters to future water availability in the global monsoon region. Sci Bull 2025(70):2312–2321. https://doi.org/10.1016/j.scib.2025.05.023
- Jin C, Wang B, Liu J (2020) Future changes and controlling factors of the eight regional monsoons projected by CMIP6 models. J Climate 33(21):9307–9326. https://doi.org/10.1175/JCLI-D-20-0 236.1
- Johnson NC, Krishnamurthy L, Wittenberg AT et al (2020) The impact of sea surface temperature biases on North American precipitation in a high-resolution climate model. J Clim 33:2427–2447. ht tps://doi.org/10.1175/JCLI-D-19-0417.1
- Kanamitsu M, Ebisuzaki W, Woollen J et al (2002) NCEP–DOE AMIP-II reanalysis (R-2). Bull Amer Meteor Soc 83:1631–1644. https://doi.org/10.1175/BAMS-83-11-1631
- Kunkel KE, Stevens LE, Stevens SE, et al (2013) Regional climate trends and scenarios for the U.S. National Climate Assessment: Part 1—Climate of the Northeast U.S. NOAA Technical Report NESDIS (vol 142–1 pp 80). https://repository.library.noaa.gov/view/noaa/56802
- Kushnir Y, Seager R, Ting M et al (2010) Mechanisms of tropical Atlantic SST influence on North American precipitation variability. J Clim 23:5610–5628. https://doi.org/10.1175/2010JCL1317
- Leathers DJ, Yarnal B, Palecki MA (1991) The Pacific/North American teleconnection pattern and United States climate. Part I: regional temperature and precipitation associations. J Climate 4:517–528. https://doi.org/10.1175/1520-0442(1991)004%3c0517:TPATPA %3e2.0.CO;2
- Li Z, Wang Y, Guo J et al (2019) East Asian study of tropospheric aerosols and their impact on regional clouds, precipitation, and climate (EAST-AIRCPC). J Geophys Res Atmos 124:13026–13054. https://doi.org/10.1029/2019JD030758
- Littell JS, Peterson DL, Riley KL et al (2016) A review of the relationships between drought and forest fire in the United States. Glob Change Biol 22:2353–2369. https://doi.org/10.1111/gcb.13275
- Liu Y, Wang H, Chen H et al (2023) Anthropogenic forcing and Pacific internal variability-determined decadal increase in summer precipitation over the Asian water tower. Npj Clim Atmos Sci 6:38. https://doi.org/10.1038/s41612-023-00369-4
- Ma W, Norris J, Chen G (2020) Projected changes to extreme precipitation along North American West Coast from the CESM large ensemble. Geophys Res Lett. https://doi.org/10.1029/2019GL08
- McCabe GJ, Palecki MA, Betancourt JL (2004) Pacific and Atlantic Ocean infuences on multidecadal drought frequency in the United States. PNAS 101:4136–4141. https://doi.org/10.1073/pnas.0306 738101
- North GR, Bell TL, Cahalan RF et al (1982) Sampling errors in the estimation of empirical orthogonal functions. Mon Weather Rev



- 110(7):699. https://doi.org/10.1175/1520-0493(1982)110%3c069 9:SEITEO%3e2.0.CO;2
- Pendergrass AG, Hartmann DL (2014) The atmospheric energy constraint on global-mean precipitation change. J Clim 27(2):757–768. https://doi.org/10.1175/JCLI-D-13-00163.1
- Plumb RA (1985) On the three-dimensional propagation of stationary waves. J Atmos Sci 42:217–229. https://doi.org/10.1175/1520-0469(1985)042%3c0217:OTTDPO%3e2.0.CO;2
- Prein AF, Rasmussen RM, Ikeda K et al (2017) The future intensification of hourly precipitation extremes. Nat Clim Change 7(1):48–52. https://doi.org/10.1038/nclimate3168
- Ren Y, Yu H, Huang J et al (2024) The projected response of the water cycle to global warming over drylands in East Asia. Earths Future 12:e2023EF004008. https://doi.org/10.1029/2023EF004008
- Ribes A, Zwiers FW, Azaïs JM et al (2017) A new statistical approach to climate change detection and attribution. Clim Dyn 48(1):367–386. https://doi.org/10.1007/s00382-016-3079-6
- Risser MD, Collins WD, Wehner MF et al (2024) Anthropogenic aerosols mask increases in US rainfall by greenhouse gases. Nat Commun 15:1318. https://doi.org/10.1038/s41467-024-45504-8
- Ruprich-Robert Y, Delworth T, Msadek R et al (2018) Impacts of the Atlantic multidecadal variability on North American summer climate and heat waves. J Clim 31:3679–3700. https://doi.org/10.11 75/JCLJ-D-17-0270.1
- Schneider U, Becker A, Finger P et al (2014) GPCC's new land surface precipitation climatology based on quality-controlled in situ data and its role in quantifying the global water cycle. Theor Appl Climatol 115:15–40. https://doi.org/10.1007/s00704-013-0860-x
- Seager R, Hoerling M (2014) Atmosphere and ocean origins of North American droughts. J Clim 27:4581–4606. https://doi.org/10.117 5/JCLI-D-13-00329.1
- Seager R, Ting M (2017) Decadal drought variability over North America:mechanisms and predictability. Curr Clim Change Rep. https://doi.org/10.1007/s40641-017-0062-1
- Seager R, Vecchi GA (2010) Greenhouse warming and the 21st century hydroclimate of southwestern North America. Proc Natl Acad Sci U S A 107(50):21277–21282. https://doi.org/10.1073/pnas.0910856107
- Seager R, Harnik N, Robinson WA et al (2005) Mechanisms of ENSOforcing of hemispherically symmetric precipitation variability. Q J R Meteorol Soc 131:1501–1527. https://doi.org/10.1256/qj.04 .96
- Slivinski LC, Compo GP, Sardeshmukh PD et al (2021) An evaluation of the performance of the Twentieth Century Reanalysis version 3. J Climate 34:1417–1438. https://doi.org/10.1175/JCLI-D-20-0 505.1
- Stephens GL, Ellis TD (2008) Controls of global-mean precipitation increases in global warming GCM experiments. J Clim 21(23):6141–6155. https://doi.org/10.1175/2008JCLI2144.1
- Sugg M, Runkle J, Leeper R et al (2020) A scoping review of drought impacts on health and society in North America. Clim Change 162:1177–1195. https://doi.org/10.1007/s10584-020-02848-6
- Sun Y, Zhang X, Zwiers FW et al (2014) Rapid increase in the risk of extreme summer heat in eastern China. Nat Clim Change 4:1082–1085. https://doi.org/10.1038/nclimate2410

- Sun Y, Zhang X, Ding Y et al (2022) Understanding human influence on climate change in China. Natl Sci Rev 9(3):nwab113. https://d oi.org/10.1093/nsr/nwab113
- Tao WK, Chen JP, Li Z et al (2012) Impact of aerosols on convective clouds and precipitation. Rev Geophys. https://doi.org/10.1029/2 011RG000369
- Trenberth KE, Shea DJ (2006) Atlantic hurricanes and natural variability in 2005. Geophys Res Lett. https://doi.org/10.1029/2006 GL026894
- Wallace J, Gutzler D (1981) Teleconnections in the geopotential height feld during the Northern Hemisphere winter. Mon Weather Rev 109:784–812. https://doi.org/10.1175/1520-0493(1981)109%3c0 784:TITGHF%3e2.0.CO;2
- Wang J, Chen Y, Tett SFB et al (2020) Anthropogenically-driven increases in the risks of summertime compound hot extremes. Nat Commun 11(1):528. https://doi.org/10.1038/s41467-019-14 233-8
- Wu M, Zhou T, Li C et al (2021) A very likely weakening of Pacific Walker circulation in constrained near-future projections. Nat Commun 12(1):6502. https://doi.org/10.1038/s41467-021-2669 3-v
- Wu X, Yeager SG, Deser C et al (2024) Predictability of tropical Pacific decadal variability is dominated by oceanic Rossby waves. Npj Clim Atmos Sci 7:292. https://doi.org/10.1038/s41612-024-00851-7
- Xu Y, Hu A (2018) How would the twenty-first-century warming influence Pacific Decadal Variability and its connection to North American rainfall: assessment based on a revised procedure for the IPO/PDO. J Climate 31:1547–1563. https://doi.org/10.1175/ JCLJ-D-17-0319.1
- Zhang X, Zwiers FW, Hegerl GC et al (2007) Detection of human influence on twentieth-century precipitation trends. Nature 448(7152):461–465. https://doi.org/10.1038/nature06025
- Zhang J, Zhao T, Dai A et al (2019) Detection and attribution of atmospheric precipitable water changes since the 1970s over China. Sci Rep 9(1):17609. https://doi.org/10.1038/s41598-019-54185-z
- Zhang W, Zhou T, Wu P (2024) Anthropogenic amplification of precipitation variability over the past century. Science 385:427–432
- Zhao M, Xie Y, Shi J et al (2025) Reversed future drying-wetting precipitation patterns over the northwestern and southeastern East Asia driven by reduced aerosol emissions. Geophys Res Lett. htt ps://doi.org/10.1029/2024GL114527

**Publisher's Note** Springer Nature remains neutral with regard to jurisdictional claims in published maps and institutional affiliations.

Springer Nature or its licensor (e.g. a society or other partner) holds exclusive rights to this article under a publishing agreement with the author(s) or other rightsholder(s); author self-archiving of the accepted manuscript version of this article is solely governed by the terms of such publishing agreement and applicable law.

